

## SPECTROSCOPIC OBSERVATIONS OF A CORONAL LOOP: BASIC PHYSICAL PLASMA PARAMETERS ALONG THE FULL LOOP LENGTH

G. R. GUPTA<sup>1</sup>, DURGESH TRIPATHI<sup>1</sup>, AND HELEN E. MASON<sup>2</sup>

<sup>1</sup> Inter-University Centre for Astronomy and Astrophysics, Post Bag-4, Ganeshkhind, Pune 411007, India; [girjesh@iucaa.ernet.in](mailto:girjesh@iucaa.ernet.in), [durgesh@iucaa.ernet.in](mailto:durgesh@iucaa.ernet.in)

<sup>2</sup> Department of Applied Mathematics and Theoretical Physics, University of Cambridge, Wilberforce Road, Cambridge CB3 0WA, UK; [h.e.mason@damtp.cam.ac.uk](mailto:h.e.mason@damtp.cam.ac.uk)

Received 2014 August 16; accepted 2014 December 23; published 2015 February 20

### ABSTRACT

Coronal loops are the basic structures of the solar transition region and corona. Understanding of the physical mechanisms behind the loop heating, plasma flows, and filling are still considered a major challenge in solar physics. The mechanism(s) should be able to supply mass to the corona from the chromosphere and to heat the plasma over 1 MK within a small distance of a few hundred kilometers from the chromosphere to the corona. This problem makes coronal loops an interesting target for detailed study. In this study, we focus on spectroscopic observations of a coronal loop observed in its full length in various spectral lines as recorded by the Extreme-ultraviolet Imaging Spectrometer on board Hinode. We derive physical plasma parameters such as electron density, temperature, pressure, column depth, and filling factors along the loop length from one footpoint to the another. The obtained parameters are used to infer whether the observed coronal loop is overdense or underdense with respect to gravitational stratification of the solar atmosphere. These new measurements of physical plasma parameters, from one footpoint to another, provide important constraints on the modeling of the mass and energy balance in coronal loops.

**Key words:** Sun: atmosphere – Sun: corona – Sun: transition region – Sun: UV radiation

### 1. INTRODUCTION

The problem of solar coronal heating has been one of the most stubborn problems in the field of astrophysics. In spite of major developments in observational capabilities and theoretical modeling, the problem remains to be fully solved. For an excellent extensive review, see, e.g., Klimchuk (2006).

Loops are considered to be the building blocks of the corona. Current observations suggest that there are different types of loops seen at different temperatures. Broadly, these loops could be divided into three groups based on their characteristic temperatures, namely fan loops ( $\leq 1$  MK), warm loops (seen at around 1 MK), and hot loops mainly seen in the core of active regions in high temperature lines (3–5 MK). However, there are numerous cooler closed loop structures observed in spectral lines such as O v and Si vii, i.e., below 1 MK, and they may not be classified as fan loops (see, e.g., Brekke et al. 1997). In addition to well-defined loop structures it has been found that there is a significant amount of diffuse emission in and around the active regions (see, e.g., Klimchuk 2006). In a recent study, Subramanian et al. (2014) showed that these regions have a characteristic temperature of about 2 MK. In fact, it has also been found that distinguishable loops have only about 20%–30% larger intensities than foreground/background diffuse emission (Del Zanna & Mason 2003; Viall & Klimchuk 2012). However, the exact quantity of diffuse emission varies depending on the contamination of the instrumental stray light. Therefore, for any coronal heating theories, it is important to explain all of these different kinds of emission from active regions. Although the loops are just above 20%–30% in brightness from the diffuse regions, they provide one of the best targets of opportunity to study the mass and energy circulation from the transition region to the corona.

In order to understand the emission of these different kinds of loop structures, it is most important to study their properties

using spectroscopy in addition to imaging. On one hand, spectroscopic techniques provide the most accurate physical parameters such as density, temperature, and flows. On the other hand, imaging can provide the time evolution of the structures. Since we are interested in understanding the emission from quiescent active regions, a study of the time evolution is extremely important to rule out any effects of solar activity phenomena such as flares, micro-flares, etc. on the observed loop structures.

Warm loops, which emanate mostly at the periphery of active regions, have been most easily detectable with instruments such as the Coronal Diagnostic Spectrometer (CDS; Harrison et al. 1995) on board the *Solar and Heliospheric Observatory (SOHO)*, TRACE (Handy et al. 1999), the Solar Terrestrial Relations Observatory (STEREO), the Extreme-Ultraviolet Imaging Spectrometer (EIS; Culhane et al. 2007) on board Hinode (Kosugi et al. 2007), and the Solar Dynamics Observatory (SDO). Therefore, warm loops have been the most extensively studied and physical plasma parameters have been measured using CDS/SOHO (see, e.g., Schmelz et al. 2001; Del Zanna & Mason 2003; Cirtain et al. 2007) and EIS/Hinode (see, e.g., Warren et al. 2008; Tripathi et al. 2009; Brooks et al. 2011; Scott et al. 2012; Brooks et al. 2013, and citations therein).

In this paper we report for the first time an analysis of a complete loop using a spectrometer, although extensive information on loop segments exists in the literature (see, e.g., Del Zanna & Mason 2003; Ugarte-Urra et al. 2005; Warren et al. 2008; Tripathi et al. 2009; Scott et al. 2012). The loop is observed with EIS/Hinode and the Atmospheric Imaging Assembly (AIA; Lemen et al. 2012) on board SDO. This observation provides us with an excellent opportunity to measure the physical parameters of the loop from one footpoint to the another, providing unique observational constraints to the

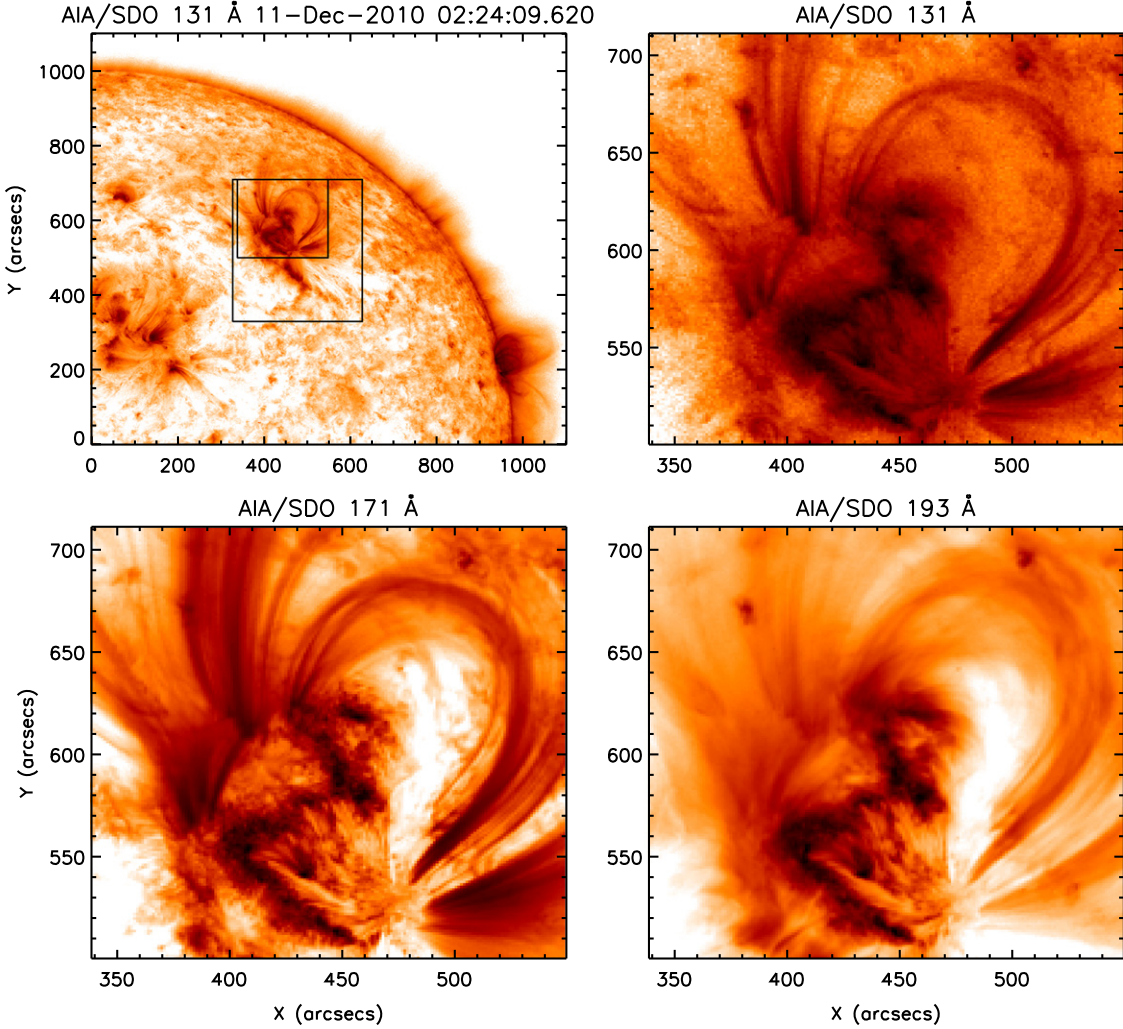


**Figure 1.** Top left image: a portion of the Sun’s disk showing the active region AR 11131 in the 131 Å passband. The bigger box indicates the region rastered by EIS/Hinode. The smaller box is shown in subsequent images taken in the AIA 131 Å, 171 Å, and 193 Å passbands, as labeled.

modeling of coronal loops. The rest of the paper is structured as follows. In Section 2 we describe the observations, followed by the data analysis and results in Section 3. We summarize our results and draw some conclusions in Section 4.

## 2. OBSERVATIONS

A coronal loop from one footpoint to another was detected in an active region, AR 11131, observed on 2010 December 11 with EIS (Culhane et al. 2007) on board Hinode (Kosugi et al. 2007). Observations were carried out with the 2'' slit with an exposure time of 35 s, and a sparse raster of the region was created with a step size of 3''. The raster scan started at 01:55 UT and was completed at 02:56 UT, covering a field of view of 384'' × 300''. We followed standard procedures for analyzing the EIS data using software available in Solar Software (SSW; Freeland & Handy 1998) to calibrate and correct for the slit tilt and orbital drift. The spatial offset in the solar Y-direction at different wavelengths was corrected by co-aligning the images at each wavelength. EIS Fe viii 186.6 Å and Mg vii 278.4 Å spectral lines were chosen to co-align the spectral images from short and long wavelength windows, as the peak formation temperature of both the lines are similar, thus revealing similar structures. The images were aligned using a cross-correlation

technique and are accurate up to a 1'' difference in the solar Y-direction; however, no spatial offset in the solar X-direction in two wavelength windows was observed, as the raster step size was 3'' in this observation.

Figure 1 provides the context image of the observed coronal loop from AIA/SDO and EIS/Hinode. The top left panel displays part of the Sun’s disk covering the active region as observed in the AIA 131 Å passband. The emission in the 131 Å passband has contributions mainly from the Fe viii, Fe xxii, and Fe xxiii spectral lines. However, for the quiescent loops Fe viii dominates the emission. For more information on dominant emission in various AIA channels in different regions, see O’Dwyer et al. (2010) and Del Zanna et al. (2011). The bigger box in the top left panel indicates the EIS raster field of view, whereas the smaller box is the part of the active region chosen for the current analysis. The chosen region clearly shows the complete coronal loop from one footpoint to another. The remaining three images correspond to the smaller box shown in the top left panel. The top right panel shows the loop in the AIA 131 Å passband, whereas the bottom panels show the AIA 171 Å (bottom left) and AIA 193 Å (bottom right) passbands. The loop structure can be identified in all the three passbands; however, the structure changes in different passbands. The AIA 131 Å passband shows a well-defined loop structure with very

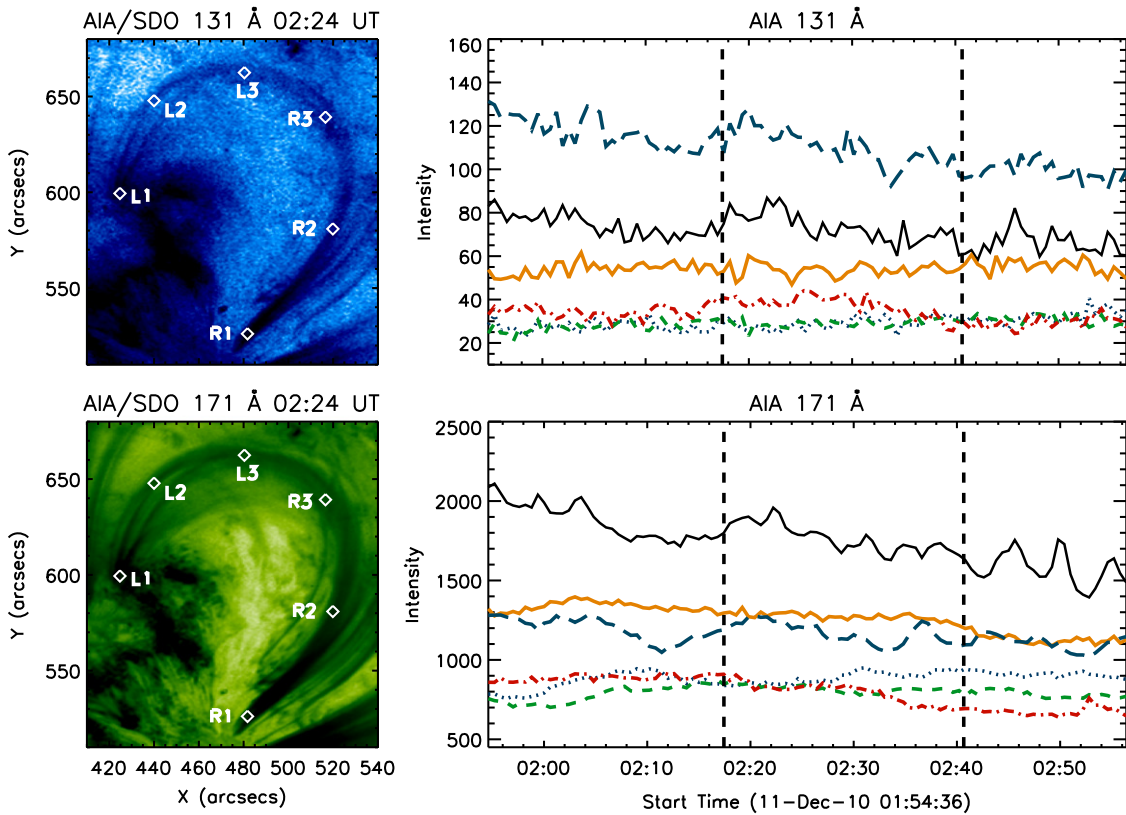


**Figure 2.** AIA 131 Å and 171 Å light curves at different locations of the coronal loop during the time interval of the EIS raster scan. The plotted curves correspond to the L1 (solid line), L2 (dotted), L3 (dashed), R3 (dot-dash-dot-dashed), and R1 (long dash) locations along the loop. The two vertical dashed lines in each panel indicate the time taken to scan the observed coronal loop using EIS.

little background/foreground emission, whereas the AIA 171 Å passband shows an enhancement in background/foreground emission. In the AIA 193 Å passband it becomes difficult to disentangle the loop structure from the foreground/background emission.

As noted by Tripathi et al. (2012), this loop is quiescent and quasi-static, and does not show any flaring and/or micro-flaring events before or after the acquired EIS raster. In order to reconfirm this, we performed a quantitative study as follows. We obtained light curves at different locations along the loop during the time interval of the EIS raster scan for AIA 131 Å and 171 Å emission. The obtained light curves, shown in Figure 2, reveal that there are no significant changes occurring during the span of the raster scan. However, a slight decrease in intensity can be observed at a few locations along with some small enhancements in the light curves. From these curves, it is plausible to conclude that within the given time scale of the raster scan the observed loop can be considered quiescent and quasi-static. This makes it a suitable observation for studying the basic plasma parameters along the full loop length.

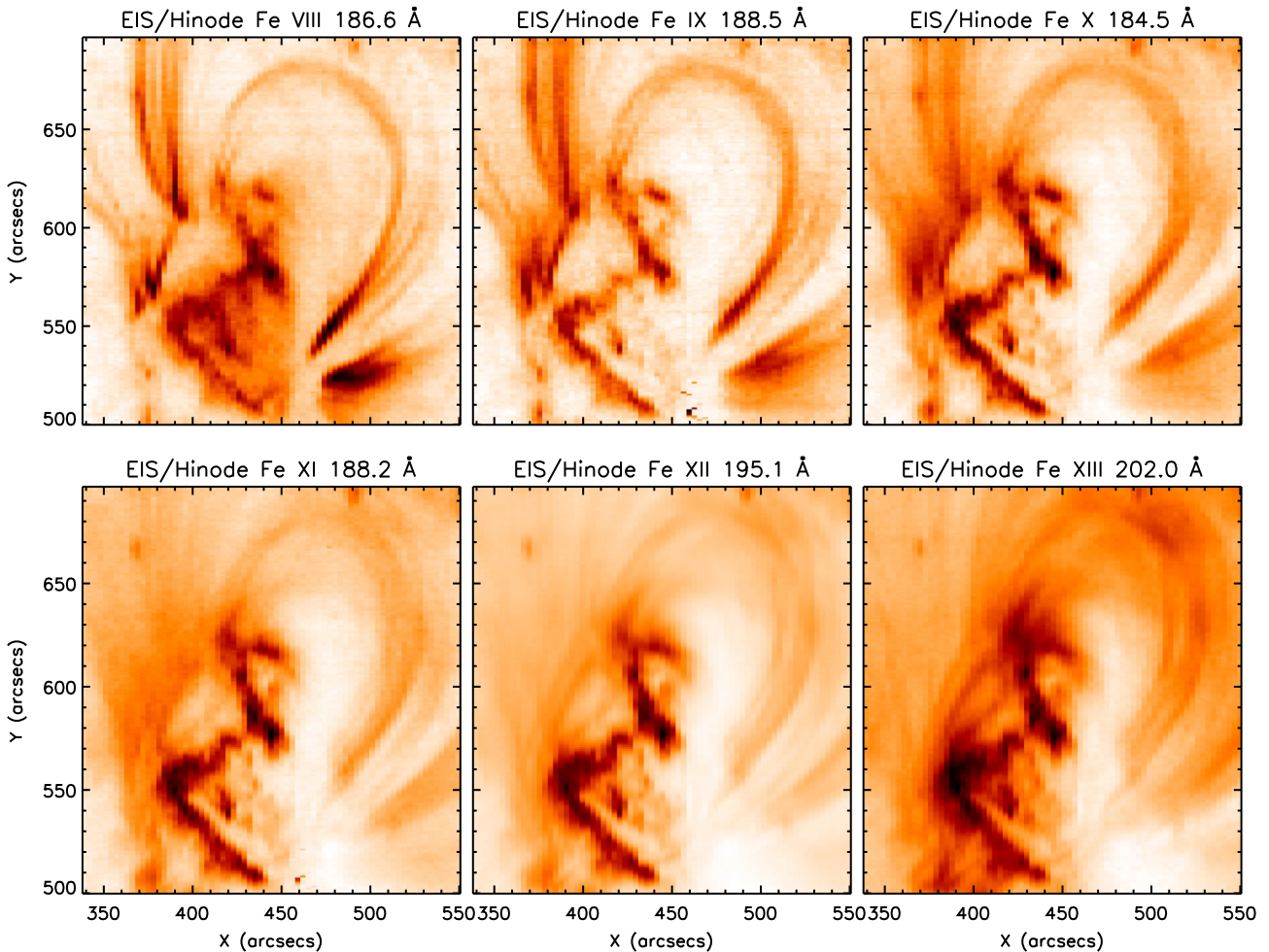
### 3. DATA ANALYSIS AND RESULTS

Figure 3 displays EIS intensity maps of the coronal loop structure obtained in different spectral lines (Fe VIII, Fe IX, Fe X, Fe XI, Fe XII, and Fe XIII) corresponding to the smaller box shown in Figure 1. The loop structure visible in the EIS Fe IX image is very similar to that seen in the AIA 171 Å passband. The loop structure becomes less distinguishable with increasing temperature. The loop can still be seen in Fe XI, where the loop intensity is still higher than the background. The loop gets

completely merged within the background/foreground in the images obtained from Fe XII and Fe XIII, showing characteristics similar to those discussed by Tripathi et al. (2009) and Guarrazi et al. (2010).

The aim of this study is to derive physical plasma parameters such as electron density, temperature, and filling factors along the loop structure. For the purpose of deriving the electron density, we have used the line pair of Mg VII  $\lambda 278.39/\lambda 280.75$ . The Mg VII 278.39 Å spectral line is blended with Si VII 278.44 Å (Young et al. 2007b). However, using the density insensitive ratio of Si VII 278.44 Å with 275.35 Å, with a fixed branching ratio of 0.32, the contribution of Si VII 278.44 Å can be removed from Mg VII 278.39 Å (Young et al. 2007a).

Figure 4 displays intensity maps showing the coronal loop obtained in the Mg VII 278.39 Å (blended with Si VII 278.44 Å), Fe VIII 186.6 Å, Fe X 184.5 Å, and Fe XII 195.12 Å (blended with Fe XII 195.18 Å) spectral lines after fitting the line profiles with a single Gaussian function. The overplotted asterisk signs in the Mg VII 278.39 Å intensity map indicate the manual tracing of the loop. The loop is also traced in other spectral lines and overplotted with dashed lines. For comparison, we overplotted the traced loop coordinates of Mg VII 278.39 Å with a continuous line on top of the intensity maps obtained from higher temperature spectral lines. These images reveal that with increasing temperature, the loop top extends to a higher altitude. The difference between the apex regions is not so large between Mg VII and Fe X, but the difference becomes significant between Mg VII and Fe XII, and is more than 7''. Since great care has been taken with the co-alignment, we believe that this is real and not due to any instrumental effects



**Figure 3.** Monochromatic intensity maps of active region AR 11131 obtained in different wavelengths using EIS/Hinode (as labeled). The maps correspond to the upper half of the box shown in the top right panel of Figure 1.

(images at different wavelengths are aligned with an accuracy of about  $1''$ ). Therefore, it is plausible to conclude that the structures seen in Fe XII are different from those seen in Mg VII.

For this analysis, we have considered the loop structure observed in Mg VII. In order to improve the signal-to-noise ratio, we binned over three pixels in the  $Y$ -direction for each of the tracked points along the loop. All the resultant profiles are fitted with a Gaussian to extract the line parameters along the loop. The contribution of Si VII 278.44 Å has been subtracted from the Mg VII 278.39 Å spectral line using the constant branching ratio of Si VII 278.44 Å with Si VII 275.3 Å.

Figure 5 shows the variation in intensity along the loop in various spectral lines as labeled in the plot. These intensities were corrected for the sensitivity degradation with time of the EIS instrument as per the scheme suggested by Del Zanna (2013). As is evident from the figure, the observed loop is brightest in the Fe VIII 186.60 Å, whereas it is barely visible in the Mg VII 280.75 Å spectral line, except for the two footpoints. The plot also suggests that the intensity at footpoint B is a factor of 4–5 larger than that at footpoint A. This is very likely caused by footpoints of various loop structures aligned along the line of sight, as can also be seen from the AIA images.

In order to estimate the height of the loop with respect to the footpoints, we use the following method. We first draw a straight line connecting the two footpoints. The lines normal to

the line connecting the two footpoints will provide the projected height extent of the loop coordinates with respect to the footprints in the *solar XY* plane. The estimated height extents of the loop points are plotted in Figure 6 and marked with asterisks. The projected loop top extends up to a height of  $\approx 85$  Mm (positions 22–23).

In order to get the exact height of the loop, we need to correct for the projection effect. This would require information on the inclination angle of the loop plane with respect to the *solar XY* plane. This is a non-trivial exercise, as we do not have observations from any other vantage points. Unfortunately, the separation angle between the two STEREO spacecraft was so large at the time of observation that only STEREO-A could see the loop. Additionally, the angle between SDO and STEREO-A was also too large to perform any stereoscopic studies. Therefore for the current analysis, we assumed that the coronal loop would be extending radially outward, and found that the loop would be inclined toward the observer at an angle of  $\sim 36^\circ$  (for an average loop location at  $X \approx 450''$ ,  $Y \approx 580''$  and a solar radius of  $\approx 980''$ ) with respect to the *solar XY* plane. In this case, the loop top would extend up to a height of  $\approx 110$  Mm (marked with diamonds in Figure 6, positions 22–23).

To estimate the basic plasma parameters along the loop, we employ methods used by Tripathi et al. (2010) and described in subsequent subsections.

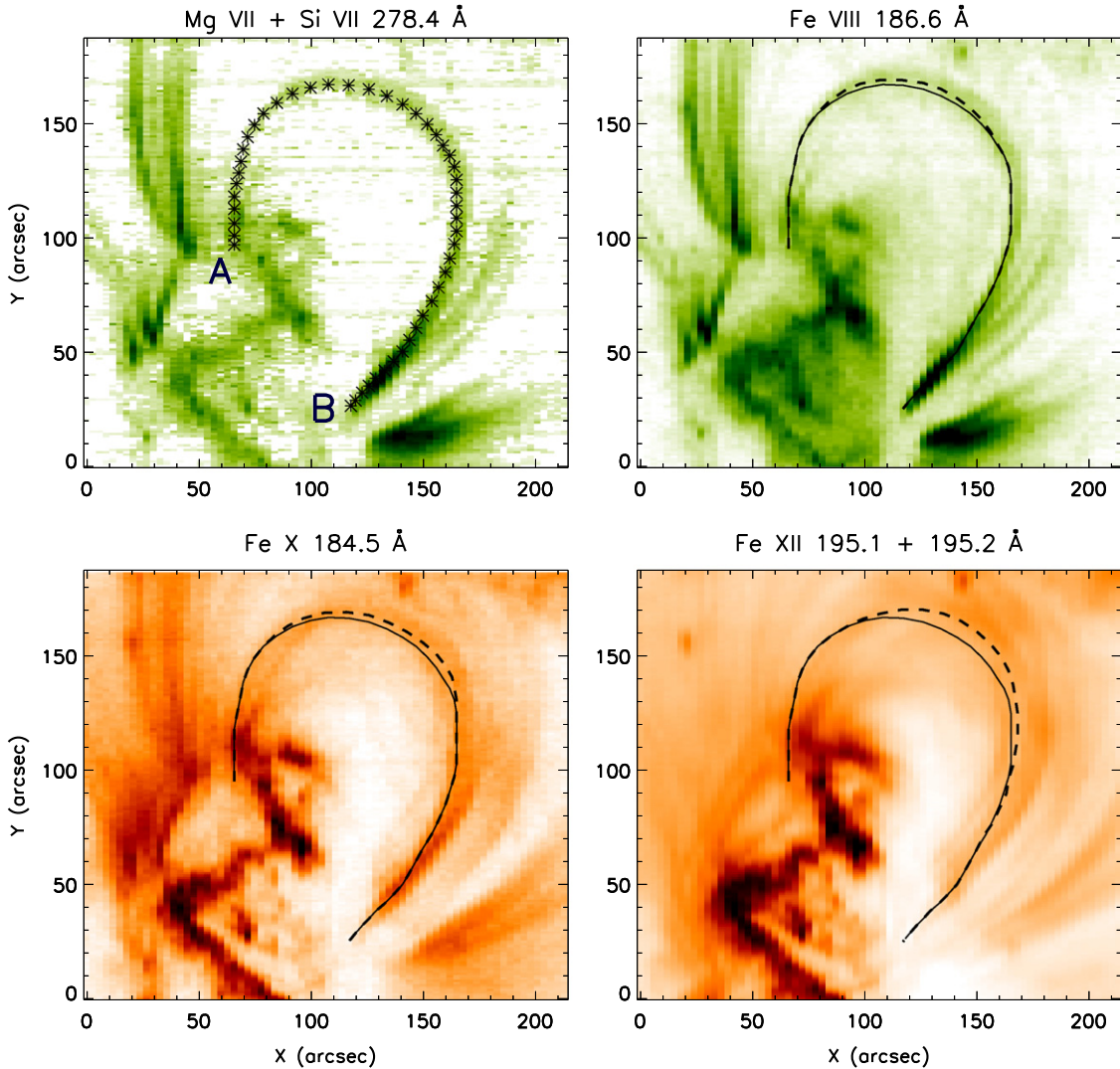


**Figure 4.** Traced coronal loop from left footpoint A to right footpoint B as seen in the Mg vii 278.39 Å (blended with Si vii 278.44 Å) spectral line (top left). The loop is also traced manually in the Fe viii 186.6 Å (top right), Fe x 184.5 Å (bottom left), and Fe xii 195.12 Å (blended with Fe xii 195.18 Å; bottom right) spectral lines, marked with dashed lines. The traced loop structure from Mg vii 278.39 Å is also overplotted with a continuous line in all of the other panels.

### 3.1. Density Along the Loop Length

The electron density of a stellar atmosphere can be derived by taking the intensity ratio of two emission lines of the same ion with a different dependence on the electron density (e.g., Mason & Monsignori Fossi 1994; Young et al. 2009). Densities obtained from this method do not depend on the emitting volume, elemental abundances, and ionization state of the plasma, and purely depend on the atomic population processes within the ion and provide the mean electron density along the line of sight.

EIS provides access to a number of density sensitive line ratios formed at different temperature ranges (Young et al. 2007b). We measured the electron number density along the full loop length using density sensitive line ratios from the different ions using CHIANTI version 7.1 (Dere et al. 1997; Landi et al. 2012). We choose a pair of Mg vii  $\lambda 278.39/\lambda 280.75$  density sensitive lines to obtain the electron density at various points along the loop length. The loop is clearly visible in the Mg vii 278.39 Å spectral line along its full length. A distinguishable structure can also be seen in Mg vii 280.75 Å; however, it is barely visible toward the loop top,

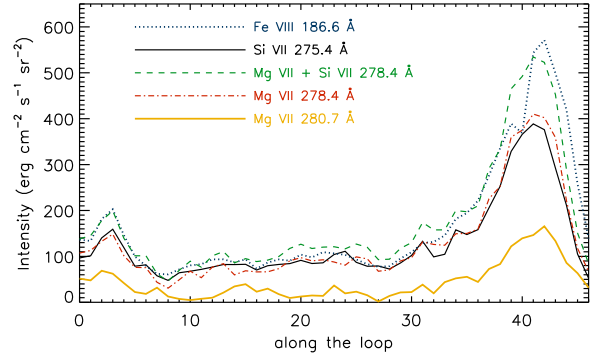


**Figure 5.** Variation in intensity along the coronal loop from left footpoint A to right footpoint B as measured in different spectral lines from EIS/Hinode.

indicating a lower electron density toward the loop top in comparison to the footpoints (see Figure 7). Therefore, as mentioned earlier, in order to obtain a good signal, we binned over three pixels in the Y-direction at all the chosen points

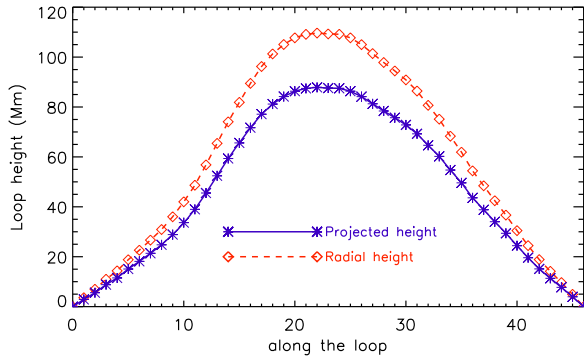


**Figure 6.** Height of the traced coronal loop from left footpoint A to right footpoint B as measured with respect to the loop footpoints and obtained from the Mg vii 278.39 Å intensity map.

along the loop so as to be able to perform the Gaussian fit and obtain the intensities in both the spectral lines.

Figure 8 shows the density variation along the loop as measured using the Mg vii line pair. We also obtained densities after performing background/foreground subtraction. However, densities before and after background subtraction do not show any significant changes, mainly due to very low background/foreground emission as can be seen from Figure 7. The density plot shows that the density drops off with the height of the loop. The number densities at both footpoints are similar and have values  $\approx 10^{9.4} \text{ cm}^{-3}$ . The density decreases upon moving toward the loop top and attains the lowest value of about  $\approx 10^{8.5} \text{ cm}^{-3}$  (see Figure 8, positions 15–16). Moving toward the loop top, the signal strength of Mg vii 280.75 Å goes down, resulting in larger error bars. As mentioned earlier, toward the loop top there is hardly any signal, thus a number density estimate toward the loop top was not possible. We will use this electron density obtained from the Mg vii line ratio for the purpose of further analysis.

### 3.2. Temperature Along the Loop Length

Basic physical plasma parameters along the loop length, such as temperature and filling factors, can be derived using spectroscopic techniques as follows.

The expression for the optically thin emission line intensity can be given as

$$I = 0.83 Ab(z) \int G(T_e, N_e) N_e^2 dh, \quad (1)$$

where  $Ab(z)$  is the elemental abundance,  $N_e$  is the electron number density,  $h$  is column depth of emitting plasma along the line of sight. The factor 0.83 is the ratio of protons to free electrons, which is a constant for temperatures above  $10^5 \text{ K}$ .  $G(T_e, N_e)$  is the contribution function which contains all the relevant atomic parameters for each spectral line and is defined as

$$G(T_e, N_e) = \frac{hc}{4\pi\lambda_{i,j}} \frac{A_{ji}}{N_e} \frac{N_j(X^{+m})}{N(X^{+m})} \frac{N(X^{+m})}{N(X)}, \quad (2)$$

where  $i$  and  $j$  are the lower and upper levels,  $A_{ji}$  is the spontaneous transition probability,  $\frac{N_j(X^{+m})}{N(X^{+m})}$  is the population of level  $j$  relative to the total  $N(X^{+m})$  number density of ion  $X^{+m}$  and is a function of electron temperature and density, and

$\frac{N(X^{+m})}{N(X)}$  is the ionization fraction and is predominantly a function of temperature. All the calculations were performed using CHIANTI version 7.1 (Landi et al. 2012, 2013) available in the SSW distribution and using the coronal abundances of Feldman (1992). The contribution functions  $G(T_e, N_e)$  of various spectral lines are plotted in Figure 9.

The column emission measure (EM) can be defined as

$$\text{EM} = \int N_e^2 dh. \quad (3)$$

Thus, the column EM can then also be written as

$$\text{EM} = \frac{I_{\text{obs}}}{0.83 Ab(z) G(T_e, N_e)}. \quad (4)$$

An estimate of the electron temperature of plasma can be obtained using emission lines from ions with different ionization stages. As contribution functions of spectral lines are highly dependent on temperatures, the observed intensity can be converted to temperature upon analyzing a broad range of ion species. An effective technique used for estimating the electron temperature is called the EM loci method (e.g., Jordan et al. 1987; Del Zanna et al. 2002). In this method, the ratios of observed intensities of different spectral lines with their corresponding contribution functions and abundances (i.e., EM as defined in Equation (4)) are plotted as a function of temperature. If the plasma is isothermal along the line of sight then all of the curves would cross at a single location, indicating a single temperature. In this study, we used density insensitive emission lines Fe viii 186.61 Å, Fe ix 188.5 Å, Si vii 275.35 Å, and Mg vii 278.39 Å to obtain the EM loci curves. We obtained EM loci curves at all locations along the loop from point A to point B as labeled in Figure 4. However, we have plotted only a few of them in Figure 10 to show the trend in temperature variation. The EM curves obtained from these spectral lines cross (or have a point of closest approach) at almost the same temperature, suggesting that the loop is nearly isothermal along its length. A similar result was found in previous studies using CDS and EIS (see, e.g., Del Zanna & Mason 2003; Warren et al. 2008; Tripathi et al. 2009).

There are in total six intersection points for all four spectral lines at each location. We took the mean of these points as the electron temperature at that location and the standard deviation of these points to be the error bar on the temperature at that location. The resultant temperature variation along the loop as obtained from the EM loci curve method is shown in Figure 11. The figure indicates that the temperature is almost constant along the loop within the obtained error bar; however, a slight decrease is observed near right footpoint B. We also obtained the average EM distribution along the loop length in a similar way, and this is shown in Figure 12. The average EM variation along the loop is similar to that of the intensity variation along the loop, as found in Figure 5. The EM loci method has been used to study temperature structure across various points along the partial loop segment by various authors using EIS data (see, e.g., Warren et al. 2008; Tripathi et al. 2009; Scott et al. 2012). Scott et al. (2012) in particular found almost a constant temperature of  $\log T = 6.2$  along a loop segment using a similar method. In this study, the average temperature along the loop length is found to be about 0.73 MK ( $\log T = 5.86$ ), as obtained from the spectral lines in which loops were clearly visible. However, we would also like to point out that Krishna Prasad et al. (2013) found a temperature gradient along the

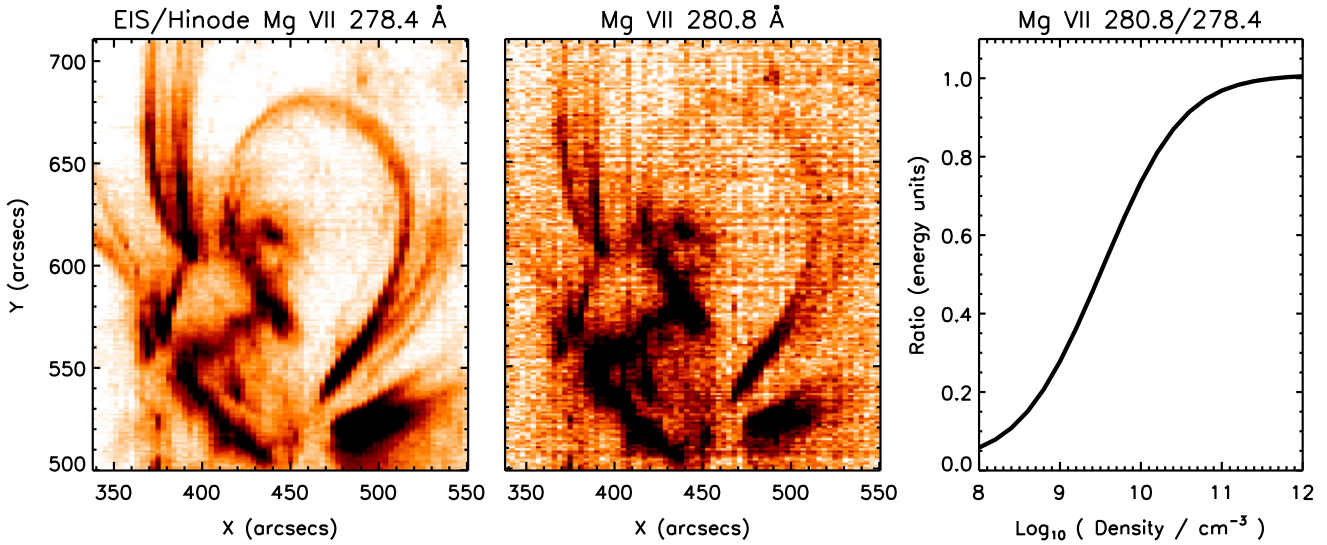


**Figure 7.** Intensity maps of the coronal loop obtained in the Mg vii 278.39 Å (left panel) and 280.75 Å (middle panel) spectral lines. The intensity ratio of the two spectral lines is sensitive to the electron density, and the variation is obtained from CHIANTI version 7.1 (right panel).

different off-limb loop structures using the temperature sensitive emission line ratio method.

As noted in Figures 8 and 11, the density decreases while the temperature remains almost steady upon moving from the loop footpoints toward the loop top. Thus, we obtained the thermal pressure along the loop using the ideal gas equation  $p = 2N_e k_b T_e$  (for the coronal pressure, the ion pressure ( $p_i$ ) and electron pressure ( $p_e$ ) are added together; Aschwanden 2005) and plotted it in Figure 13. We see that the pressure at left footpoint A ( $p \approx 0.5 \text{ g cm}^{-3} \text{ s}^{-2}$ ) is slightly higher than that at right footpoint B ( $p \approx 0.4 \text{ g cm}^{-3} \text{ s}^{-2}$ ). However, the measured pressure differences at the two footpoints are very small and may arise due to small evolutionary changes in the loop during the raster scan.

### 3.3. Filling Factor Along the Loop Length

Knowledge of the coronal filling factor ( $\phi$ ), which is a ratio of the volume radiating in X-rays and EUV to the total volume, is an important parameter in order to understand the coronal heating (Cargill 1993). This provides information on whether the observed structures are resolved or unresolved with the given instrument. Almost all of the one-dimensional hydrodynamic models require coronal structures observed with current day instrumentation to be multi-stranded in order to explain the observations (Klimchuk 2006). Therefore, a clear understanding of filling factors would provide crucial inputs to the theoretical modeling of coronal structures and thereby would help us understand the coronal heating problem better. We estimate the filling factor along the coronal loop using a process similar to that of Tripathi et al. (2010) and described below.

As noted earlier, the EM can be estimated using two different methods (Equations (3) and (4)). Thus, the plasma filling factor ( $\phi$ ) can be obtained from (Cargill & Klimchuk 1997; Tripathi et al. 2010)

$$\phi = \frac{\text{EM}}{N_e^2 h}, \quad (5)$$

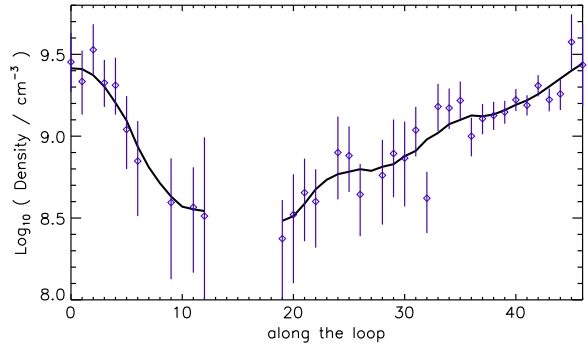


**Figure 8.** Density measured along the coronal loop from left footpoint A to right footpoint B using the Mg vii  $\lambda 280.75/\lambda 278.39$  line ratio. The five-point running average of data points is also overplotted with a continuous line.

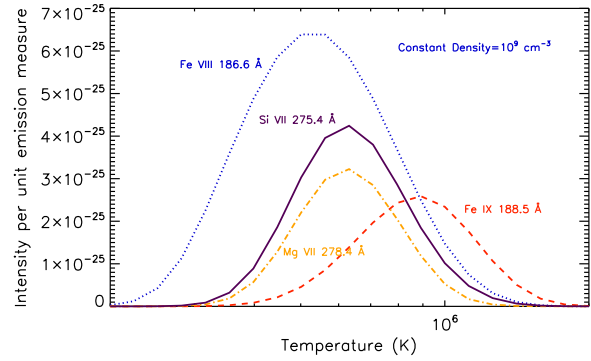


**Figure 9.** Contribution functions of various spectral lines as labeled and used in this study.

where the EM is measured using Equation (4) and  $N_e$  is measured in Section 3.1.

The most important parameter, therefore, is to estimate the column depth  $h$  from observations in order to estimate the filling factors. In this case, the column depth at each position was measured assuming that the loop has a cylindrical geometry. Thus, the projected loop diameter (geometric width of the loop) will be equal to the column depth ( $h$ ). We estimate the loop diameter to be equal to the FWHM obtained after

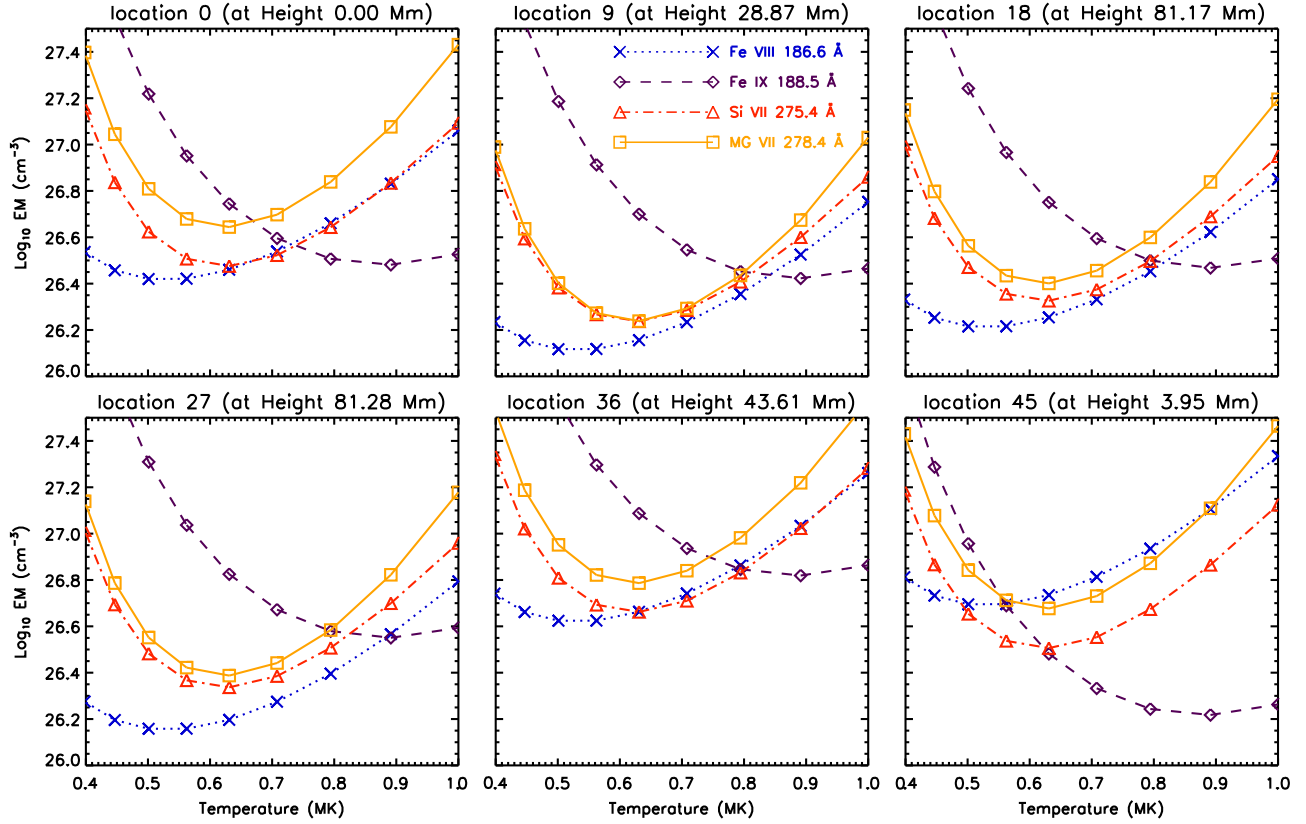


**Figure 10.** EM loci curves of several spectral lines obtained at various locations along the coronal loop.

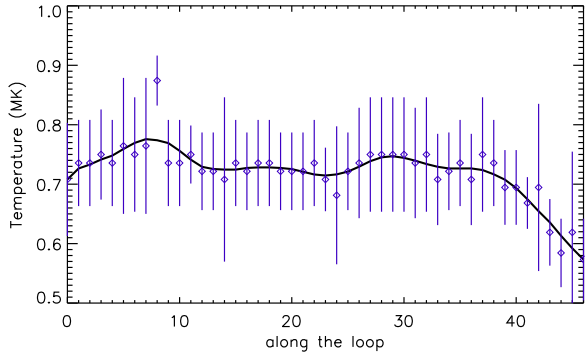


**Figure 11.** Temperature variation along the coronal loop from left footpoint A to right footpoint B as obtained from the EM loci curves. The five-point running average of the data points is also overplotted with a continuous line.

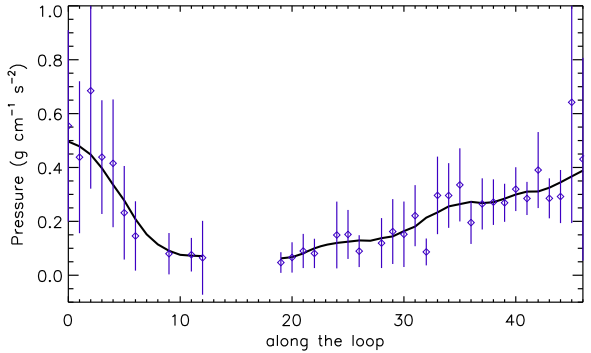


**Figure 13.** Pressure variation along the coronal loop from left footpoint A to right footpoint B as obtained from the ideal gas equation. The five-point running average of the data points is also overplotted with a continuous line.

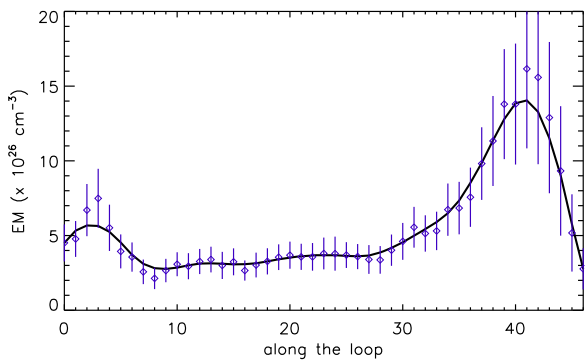


**Figure 12.** Average EM variation along the coronal loop from left footpoint A to right footpoint B as obtained from the EM loci curves. The five-point running average of the data points is also overplotted with a continuous line.

fitting a Gaussian function across the loop points. The estimated column depth, which is the geometric width of the loop along the loop length, is plotted in Figure 14. We obtained the geometric width of the loop in several spectral lines in which the loop is clearly visible. The plot shows many fluctuations in the loop width, which can also be seen in the intensity maps. The average loop width is almost constant as we move from left footpoint A, and increases toward the loop top and decreases further after attaining a maximum width at the loop top (see Figure 14, positions 15–16). Toward the right loop footpoint B, the loop width again increases. This increase in the loop width is due to the fact that there are many more structures emanating from that location that are aligned along the loop, as can be seen in the images recorded by AIA/SDO and as shown in Figure 1. We will use this average loop width along the loop length for further analysis in this study. It is also

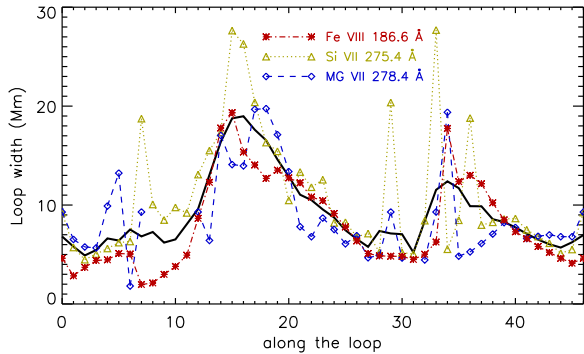


**Figure 14.** Geometric width of the coronal loop from left footpoint A to right footpoint B as seen in different spectral lines. The dark continuous line provides the average width obtained from different spectral lines along the loop length.

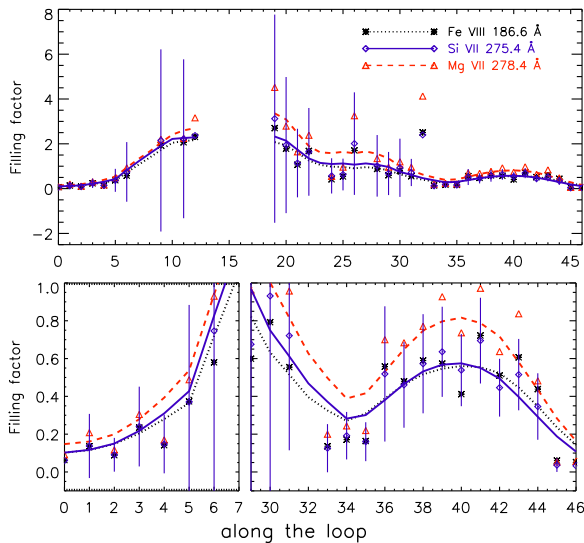


**Figure 15.** Plasma filling factor ( $\phi$ ) along the coronal loop from left footpoint A to right footpoint B as measured in different spectral lines. The five-point running average of the data points is also overplotted.

interesting to note that the loop width has increased by a factor of about two between the tracked points 10 and 16. This may indicate that the observed loop may not have a cylindrical geometry, and has a different orientation angle along the loop with respect to the line of sight. However, we will keep assuming a cylindrical geometry of the loop for further analysis in this study.

To obtain the plasma filling factors ( $\phi$ ) from various spectral lines using Equation (5), we used the densities obtained from the Mg vii line ratio along the loop length and the average loop width obtained from different spectral lines, and the EM value (from Equation (4)) is used for the corresponding loop temperature at that location as found in Figure 11. The plasma filling factors obtained from different spectral lines along the loop length are plotted in Figure 15. Error bars on filling factors were obtained from standard procedures that include errors on density, EM, and loop width ( $1\sigma$  error on FWHM) measurements. As is evident from the plot shown in the top panel of Figure 15, the filling factor values goes to 2, which is unrealistic. This is mainly the case near the loop top regions where errors on the estimation of the column depth as well as the determination of electron density are rather large due to a very small signal-to-noise ratio. In the bottom two plots of

Figure 15, we have taken the left segment and right segment of the loop separately until the height where the filling factor measurements could be considered real. These plots suggest that the filling factor increases as one moves from the loop footpoint to the loop top. Filling factors at the left footpoint A are about 0.11 (11%), 0.11 (11%), and 0.16 (16%) as measured using the intensities from the Fe viii, Si vii, and Mg vii spectral lines, respectively. The filling factor again decreases in all spectral lines while approaching right footpoint B. However, it is observed that near footpoint B, there are local enhancements in the filling factors in all spectral lines, and this might have resulted from the appearance of other structures along the line of sight (which results in an underestimation of the column depth), as is also evident from the intensity images obtained from EIS rasters as well as AIA images (see Figure 4).

The increase in filling factor values along the loop until the height at which it can be reliably measured is probably a consequence of the decrease in density (it depends on the square of the density, Equation (5)) and can be considered real within the given error bars. Note that the filling factor values obtained here are lower than those reported by Brooks et al. (2012; for the loops with temperatures of about  $\log T = 6.2$ ), especially toward the footpoint regions. As mentioned earlier, the loop geometry may not be cylindrical; thus, our assumption of a cylindrical geometry may have some effect on the filling factor measurement. However, within the obtained error bars, this effect is likely to be very small.

#### 3.4. Comparison with Hydrostatic Equilibrium

The unique observation and measurement of density and temperature along a complete coronal loop made it possible to compare the loop parameters with hydrostatic equilibrium. This has been done in the past with observations recorded using TRACE (e.g., Aschwanden 2000), but has never been done using spectroscopic observations.

The electron density profile for a loop in hydrostatic equilibrium is given by

$$n_e(h) = n_e(0) \exp\left(-\frac{h}{\lambda(T_e)}\right), \quad (6)$$

where  $\lambda$  is the density scale height given by

$$\lambda(T_e) = \frac{k_b T_e}{\mu m_H g} \approx 46 \left[ \frac{T_e}{1 \text{ MK}} \right] [\text{Mm}], \quad (7)$$

where  $k_b$  is the Boltzmann constant,  $T_e$  is the electron temperature,  $\mu$  is the mean molecular weight ( $\approx 1.4$  for the solar corona),  $m_H$  is the mass of the hydrogen atom, and  $g$  is the acceleration due to gravity at the solar surface (see, e.g., Aschwanden et al. 1999).

Figure 16 displays the variation of electron density with height, as obtained from the Mg vii line pair, with diamonds and the five-point running average of the densities with a solid black line. We compare the density variation with height in the loop as obtained from the Mg vii line pair with an exponentially decreasing density profile as given by Equation (6). The density scale height was calculated for an electron temperature of 0.73 MK as obtained from the EM loci method. We compare the density variation with the projected (dashed line) and radially directed loop heights (dot-dot-dashed line) as shown in Figure 16. Figure 16 indicates that the observed density does

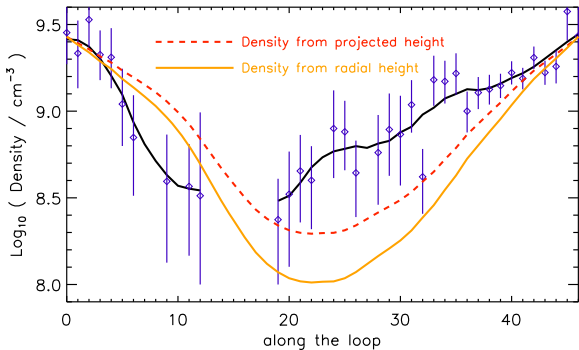


**Figure 16.** Comparison of density as measured using the Mg vii  $\lambda 280.75/\lambda 278.39$  line ratio (plotted with a diamond symbol) and five-point running average (plotted with a continuous line) from left footpoint A to right footpoint B with the density expected from a hydrostatic model at temperature 0.73 MK obtained from projected (dashed line) and radial (dot-dashed line) heights of the loop as found in Figure 6.

not fall off with height as expected from the hydrostatic model. Although the density decreases with height, the fall is different from the expected hydrostatic equilibrium model. The comparison shows that left half of the loop is underdense, whereas the right half of the loop is overdense. This result will also hold true in the case of the loop being inclined away or toward the observer with respect to the solar XY plane within an angle of  $36^\circ$ . Thus, we suggest that the observed loop has a non-symmetric density distribution as compared to the hydrostatic equilibrium and isothermal model.

#### 4. DISCUSSIONS AND SUMMARY

Using the EIS/Hinode observations, we have studied the basic physical plasma parameters such as electron density, column depth, filling factors, temperature, and thermal pressure along a coronal loop from one footpoint to another. So far, studies regarding coronal loops using spectrometers have been performed on small loop segments (see, e.g., Schmelz et al. 2001; Del Zanna & Mason 2003; Cirtain et al. 2007; Warren et al. 2008; Tripathi et al. 2009). The measurements reported here make this paper unique, as these parameters are derived from one footpoint to another. Moreover, these measurements have allowed us to perform a comparison, for the first time, of the observed loop properties with the hydrostatic equilibrium obtained using spectroscopic data.

The results obtained are summarized below.

1. Using the spectral line ratios of Mg vii  $\lambda 278.39/\lambda 280.75$ , we derived electron densities along the loop length. The result indicates a fall of density from the loop footpoint to the loop top; the density measured at the loop footpoints is about  $10^{9.4} \text{ cm}^{-3}$ , which decreases to about  $10^{8.5} \text{ cm}^{-3}$  toward the loop top.
2. We obtained the temperature of the observed loop, both across (along the line of sight) and along the loop length using the EM loci method. We found that the loop is almost isothermal across and along the loop, with a temperature of about 0.73 MK.
3. We measured the diameter of the loop along its length using the images obtained in different spectral lines and found that the loop has a non-uniform cross section (see Figure 14; see also Dudík et al. 2014). We also estimated filling factors along the loop length and found that the

values obtained are similar to those reported previously. The filling factors obtained using the Mg vii 278.4 Å, Si vii 275.4 Å, and Fe viii 186.6 Å spectral lines are similar to each other within  $\sim 10\%$  (which increases with height) of the error bars. This is not surprising as the peak formation temperature for all three lines is the same. Therefore, it is plausible to infer that the loop is multi-stranded.

4. The electron density obtained along the coronal loop from the Mg vii line pair is compared with the hydrostatic equilibrium model at an isothermal temperature of 0.73 MK as was obtained from the EM loci study. We found that the observed densities in the left segment of the loop were lower (i.e., underdense) than that expected from the isothermal hydrostatic model. However, it was higher (i.e., overdense) for the right segment of the loop (see Figure 16). This suggests a non-symmetric density profile along the loop. However, we emphasize that this result is obtained under the assumption that the observed loop is extending radially outward and will also hold true if the loop is inclined not only toward but also away from the observer with respect to the solar XY plane within an angle of  $36^\circ$ .

The results obtained here for the complete loop provide an opportunity for comparison with various loop models. The near isothermal nature of the loop along with the small filling factor and overdensity (super-hydrostatic) are in agreement with the impulsive heating model (Cargill & Klimchuk 2004; Klimchuk 2006). However, the observations presented here show the overdensity in only one part of the loop. However, the quasi-steady footpoint heating model, which drives the thermal non-equilibrium solutions, may explain the observed properties of the loop studies here (e.g., Lionello et al. 2013; Mikić et al. 2013); however, see Klimchuk et al. (2010), Tripathi & Klimchuk (2013), and Klimchuk & Bradshaw (2014). Therefore, it will be interesting and important to measure physical properties such as densities, flows, and geometries of many well-observed coronal loops and compare their properties with various loop heating models to make generic conclusive statements on their heating and dynamics.

We acknowledge useful discussions at the International Space Science Institute (ISSI) workshops on “Active Region Heating.” We thank the referee for helpful comments and suggestions that have improved the quality of our article. G.R.G. is supported through the INSPIRE Faculty Fellowship of the Department of Science and Technology (DST), India. H. E.M. acknowledges financial support from STFC (UK). Hinode is a Japanese mission developed and launched by ISAS/JAXA, collaborating with NAOJ as a domestic partner and NASA and STFC (UK) as international partners. Scientific operation of the Hinode mission is conducted by the Hinode science team organized at ISAS/JAXA. This team mainly consists of scientists from institutes in the partner countries. Support for the post-launch operation is provided by JAXA and NAOJ (Japan), STFC (UK), NASA (USA), ESA, and NSC (Norway). The data used here are courtesy of NASA/SDO and the AIA consortium.

#### REFERENCES

- Aschwanden, M. J. 2005, Physics of the Solar Corona. An Introduction with Problems and Solutions (2nd ed.; Chichester: Praxis Publishing Ltd; New York: Springer)

- Aschwanden, M. J., Newmark, J. S., Delaboudinière, J., et al. 1999, *ApJ*, **515**, 842
- Aschwanden, M. J., Nightingale, R. W., & Alexander, D. 2000, *ApJ*, **541**, 1059
- Brekke, P., Kjeldseth-Moe, O., & Harrison, R. A. 1997, *SoPh*, **175**, 511
- Brooks, D. H., Warren, H. P., & Ugarte-Urra, I. 2012, *ApJL*, **755**, L33
- Brooks, D. H., Warren, H. P., Ugarte-Urra, I., & Winebarger, A. R. 2013, *ApJL*, **772**, L19
- Brooks, D. H., Warren, H. P., & Young, P. R. 2011, *ApJ*, **730**, 85
- Cargill, P. J. 1993, *SoPh*, **147**, 263
- Cargill, P. J., & Klimchuk, J. A. 1997, *ApJ*, **478**, 799
- Cargill, P. J., & Klimchuk, J. A. 2004, *ApJ*, **605**, 911
- Cirtain, J. W., Del Zanna, G., DeLuca, E. E., et al. 2007, *ApJ*, **655**, 598
- Culhane, J. L., Harra, L. K., James, A. M., et al. 2007, *SoPh*, **243**, 19
- Del Zanna, G. 2013, *A&A*, **555**, A47
- Del Zanna, G., Landini, M., & Mason, H. E. 2002, *A&A*, **385**, 968
- Del Zanna, G., & Mason, H. E. 2003, *A&A*, **406**, 1089
- Del Zanna, G., O'Dwyer, B., & Mason, H. E. 2011, *A&A*, **535**, A46
- Dere, K. P., Landi, E., Mason, H. E., Monsignori Fossi, B. C., & Young, P. R. 1997, *A&AS*, **125**, 149
- Dudík, J., Dzifčáková, E., Cirtain, J. W., et al. 2014, *ApJ*, **796**, 20
- Feldman, U. 1992, *PhyS*, **46**, 202
- Freeland, S. L., & Handy, B. N. 1998, *SoPh*, **182**, 497
- Guarrasi, M., Reale, F., & Peres, G. 2010, *ApJ*, **719**, 576
- Handy, B. N., Acton, L. W., Kankelborg, C. C., et al. 1999, *SoPh*, **187**, 229
- Harrison, R. A., Sawyer, E. C., Carter, M. K., et al. 1995, *SoPh*, **162**, 233
- Jordan, C., Ayres, T. R., Brown, A., Linsky, J. L., & Simon, T. 1987, *MNRAS*, **225**, 903
- Klimchuk, J. A. 2006, *SoPh*, **234**, 41
- Klimchuk, J. A., & Bradshaw, S. J. 2014, *ApJ*, **791**, 60
- Klimchuk, J. A., Karpen, J. T., & Antiochos, S. K. 2010, *ApJ*, **714**, 1239
- Kosugi, T., Matsuzaki, K., Sakao, T., et al. 2007, *SoPh*, **243**, 3
- Krishna Prasad, S., Singh, J., & Ichimoto, K. 2013, *ApJL*, **765**, L46
- Landi, E., Del Zanna, G., Young, P. R., Dere, K. P., & Mason, H. E. 2012, *ApJ*, **744**, 99
- Landi, E., Young, P. R., Dere, K. P., Del Zanna, G., & Mason, H. E. 2013, *ApJ*, **763**, 86
- Lemen, J. R., Title, A. M., Akin, D. J., et al. 2012, *SoPh*, **275**, 17
- Lionello, R., Winebarger, A. R., Mok, Y., Linker, J. A., & Mikić, Z. 2013, *ApJ*, **773**, 134
- Mason, H. E., & Monsignori Fossi, B. C. 1994, *A&ARv*, **6**, 123
- Mikić, Z., Lionello, R., Mok, Y., Linker, J. A., & Winebarger, A. R. 2013, *ApJ*, **773**, 94
- O'Dwyer, B., Del Zanna, G., Mason, H. E., Weber, M. A., & Tripathi, D. 2010, *A&A*, **521**, A21
- Schmelz, J. T., Scopes, R. T., Cirtain, J. W., Winter, H. D., & Allen, J. D. 2001, *ApJ*, **556**, 896
- Scott, J. T., Martens, P. C. H., & McKenzie, D. E. 2012, *SoPh*, **276**, 113
- Subramanian, S., Tripathi, D., Klimchuk, J. A., & Mason, H. E. 2014, *ApJ*, **795**, 76
- Tripathi, D., & Klimchuk, J. A. 2013, *ApJ*, **779**, 1
- Tripathi, D., Mason, H. E., Del Zanna, G., & Bradshaw, S. 2012, *ApJL*, **754**, L4
- Tripathi, D., Mason, H. E., Del Zanna, G., & Young, P. R. 2010, *A&A*, **518**, A42
- Tripathi, D., Mason, H. E., Dwivedi, B. N., Del Zanna, G., & Young, P. R. 2009, *ApJ*, **694**, 1256
- Ugarte-Urra, I., Doyle, J. G., Walsh, R. W., & Madjarska, M. S. 2005, *A&A*, **439**, 351
- Viall, N. M., & Klimchuk, J. A. 2012, *ApJ*, **753**, 35
- Warren, H. P., Ugarte-Urra, I., Doschek, G. A., Brooks, D. H., & Williams, D. R. 2008, *ApJL*, **686**, L131
- Young, P. R., Del Zanna, G., Mason, H. E., et al. 2007a, *PASJ*, **59**, 727
- Young, P. R., Watanabe, T., Hara, H., & Mariska, J. T. 2009, *A&A*, **495**, 587
- Young, P. R., Del Zanna, G., Mason, H. E., et al. 2007b, *PASJ*, **59**, 857